energies

MDPI

Article

Characteristics of Partial Discharge of Typical Defects in Converter Transformer Under Operation

Yunpeng Tang [1], Yiming Hu [2], Hong Liu [3], Jian Liu [1], Hua Yu [3] and Minghe Chi [2,*]

[1] North China Branch of State Grid Corporation of China, Beijing 100053, China
[2] School of Electrical and Electronic Engineering, Harbin University of Science and Technology, Harbin 150080, China
[3] State Grid Shanxi Electric Power Research Institute, Taiyuan 030001, China
* Correspondence: chiminghe1985@hrbust.edu.cn; Tel.: +86-13766966488

Abstract

Converter transformers, operating in complex electric fields for extended periods, are prone to insulation degradation. To investigate partial discharge (PD) characteristics caused by internal insulation deterioration, this study developed an AC/DC PD simulation platform replicating real-world operating conditions. Four typical insulation defects—turn-to-turn, spacer block, electrostatic ring, and tap changer—were modeled, with experiments conducted in a 35 kV transformer tank using pure AC and composite AC/DC voltages (1:1, 1:3, 1:5, 1:7 ratios). The 48 Phase-Resolved Partial Discharge (PRPD) spectra were processed through image cropping, grayscale conversion, and dimension standardization, with 84% training and 16% testing datasets. Convolutional neural networks (CNNs) achieved an overall classification accuracy of 93.7% on the test set. Field validation using ±400 kV real-world converters confirmed the network's precision in PD pattern recognition, providing technical support for insulation condition diagnosis and fault prediction in converter transformers.

Keywords: converter transformer; partial discharge; combined AC/DC voltage; convolutional neural network

1. Introduction

Converter transformers are among the most critical pieces of equipment in power grids, and their operational reliability is directly related to the security and stability of power systems under the carbon peaking and carbon neutrality goals [1–3]. During long-term operation, the internal oil-paper insulation system of a converter transformer is subjected to multiple stresses, including electrical, thermal, and mechanical stresses. As a result, aging, moisture ingress, impurities, and manufacturing defects may induce PD, which in turn accelerates insulation degradation and forms a vicious cycle [4,5]. Previous studies have shown that a considerable proportion of transformer failures are caused by insulation defects [6–9]. Compared with conventional transformers, converter transformers are continuously exposed to combined AC/DC electric fields and operate under more severe conditions, leading to a higher risk of failure. Therefore, effective PD detection should be carried out for converter transformers so that potential defects can be identified and eliminated before catastrophic failures occur.

In recent years, researchers worldwide have conducted extensive studies on PD in converter transformers, which can be broadly categorized into three aspects: insulation

Check for updates

Academic Editor: Ramon Leyva

Received: 11 September 2026
Revised: 29 September 2026
Accepted: 13 October 2026
Published: 16 October 2026

Copyright: © 2026 by the authors. Licensee MDPI, Basel, Switzerland. This article is an open access article distributed under the terms and conditions of the Creative Commons Attribution (CC BY) license.

aging mechanisms, hardware denoising and signal conditioning, and machine learning-based pattern recognition. Regarding insulation aging mechanisms and field distribution, Sun et al. [10] developed a 3D model of an HVDC converter transformer to analyze the electrical field of windings subject to voltage harmonics. Dong et al. [11] studied the aggregation characteristics of metal particles and PD behavior in transformer oil under AC/DC composite voltage. Qian et al. [12] analyzed the characteristic parameters of PD and the Weibull failure characteristics of breakdown voltage in oil-paper insulation systems, providing a reference for electrical aging lifetime analysis. Le et al. [13] proposed a simulation-based method to optimize the regulating winding structure, developing an insulation structure with improved performance. In terms of hardware denoising, signal conditioning, and on-site localization, Li et al. [14] proposed an adaptive weighted framed sparse representation denoising method to effectively extract PD signals under severe noise contamination. Qu et al. [15] designed a signal conditioning circuit capable of denoising, filtering, and amplifying detected signals. For on-site applications, Li et al. [16] investigated the localization and diagnosis of PD faults in UHV converter transformers. Shao et al. [17] simulated the electromagnetic wave propagation law of PD in valve-side bushings, while Jia et al. [18] researched PD localization methods under complex multipath propagation conditions. Wei et al. [19] also proposed an on-site PD testing technique to address high test current and insufficient power supply capacity issues. For machine learning-based pattern classification algorithms, Liu et al. [20] applied cluster-based identification for DC PD defects, and Wen et al. [21] achieved defect pattern recognition based on PD characteristics for UHVDC converter transformers. Wei et al. [22] contributed to PD image feature-based defect diagnosis. D. Karthik Prabhu et al. [23] introduced a residual pooling structure to enhance feature extraction. Zhang et al. [24] proposed a data augmentation scheme based on a generative adversarial network (GAN), and Zhang et al. [25] applied the online sequential extreme learning machine (OS-ELM) algorithm. Furthermore, Chen et al. [26] proposed a multi-channel convolutional neural network (CNN) method, improving recognition accuracy by up to 30% compared with single-channel CNNs.

Despite extensive research on PD signal processing and pattern recognition, there remain significant knowledge gaps. Most existing studies rely on simplified laboratory models under single or limited voltage conditions, and comprehensive datasets covering varying AC/DC composite ratios (from 1:1 to 1:7) are still lacking. More importantly, the practical engineering applicability of intelligent diagnostic models under severe on-site electromagnetic interference has rarely been validated using real converter transformers. To fill these gaps, this study constructs a dedicated AC/DC PD simulation platform and establishes a comprehensive dataset of 48 PRPD spectra covering four typical insulation defects under various voltage ratios. A CNN-based model is then developed for automatic defect classification. The main contributions of this work are threefold: (1) the PD characteristics of four typical defects under varying AC/DC composite voltage ratios are systematically investigated; (2) a CNN-based recognition model is proposed and achieves high accuracy in laboratory tests; and (3) most importantly, the trained model is applied to a real ±400 kV converter transformer for field validation, confirming its engineering applicability. The remainder of this paper is organized as follows. Section 2 introduces the experimental platform, sample preparation, and PD signal acquisition. Section 3 details the CNN architecture and the laboratory-based PD feature recognition results. Section 4 presents the field case analysis, focusing on the field-tested PRPD patterns and the practical diagnostic performance on the ±400 kV converter transformer. Finally, Section 5 concludes the paper and discusses future work.

2. Experimental Methods

2.1. Experimental Platform

To simulate theactual operating environment of a converter transformer, the experiment was conducted in a high-voltage laboratory with ambient noise. The PD testing system was established as shown in Figure 1. The system can be used to carry out tests under pure AC voltage and AC/DC superimposed voltages with different proportions. It mainly consists of a voltage regulator (T_0), AC voltage sources (T_1,T_3), DC voltage sources (T_2, T_4), high-voltage silicon stacks (D_1, D_2), a partial-discharge-free DC-blocking capacitor (C_2), a protective resistor (R_2), and voltage dividers composed of (R_HC_H,R_LC_L).

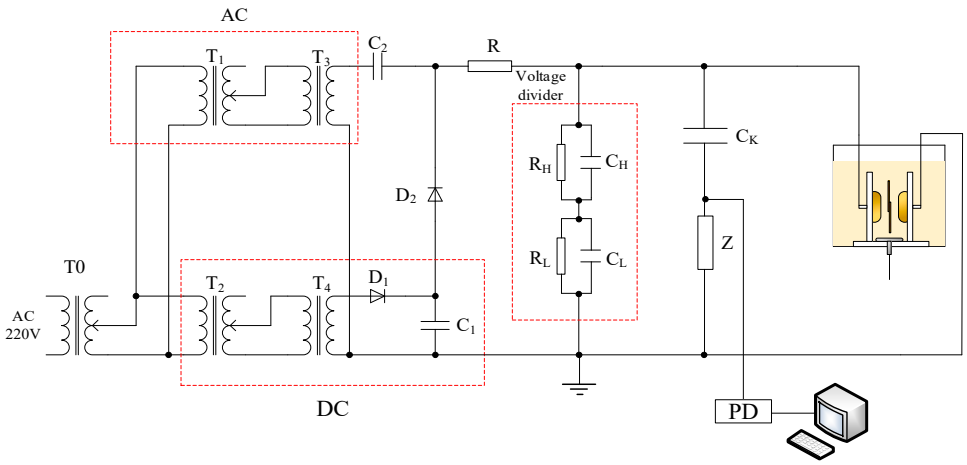


Figure 1. Schematic diagram of AC/DC combined circuit. The red dashed boxes indicate the AC power supply, DC power supply, and voltage divider, respectively. The light-yellow shaded area represents the transformer insulating oil in the test tank.

The above PD testing platform enables regulation of the DC component while maintaining a constant AC/DC voltage ratio during the voltage-raising process. In this way, the AC and DC components are increased simultaneously, thereby reproducing the voltage variation characteristics of a converter transformer under actual operating conditions.

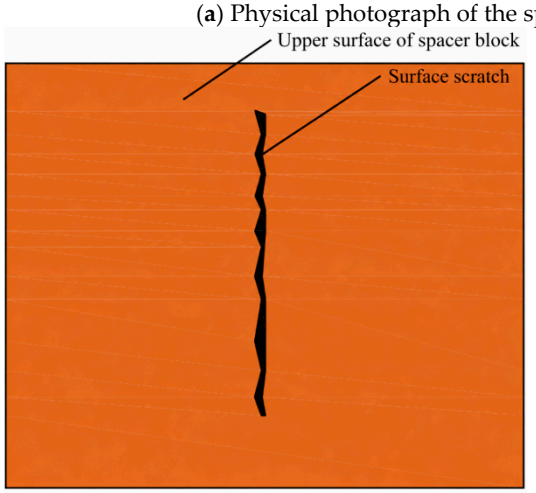
2.2. Preparation of Test Samples

Based on the actual operating conditions of converter transformers, the internal insulation materials of converter transformers were used in this study. According to their real structural characteristics, four types of laboratory models were prepared to simulate four typical insulation degradation defects in converter transformers, namely defects associated with spacers, inter-turn insulation, tap changers, and electrostatic rings.

For spacer insulation degradation defects, pressboard made of the same material as the internal spacers of converter transformers was used in the experiment. Scratches and cracks were introduced on the surface of the pressboard to simulate aging-induced cracking of spacers caused by mechanical stress, as shown in Figure 2a. Its schematic diagram is shown in Figure 2b. The electrode configuration used in the test is shown in Figure 3a. Its schematic diagram is shown in Figure 3b. A three-electrode system was employed to investigate the deterioration degree and influence mechanism of the spacer surface and ramp structure under two different electric-field conditions, namely the normal and tangential electric-field components.

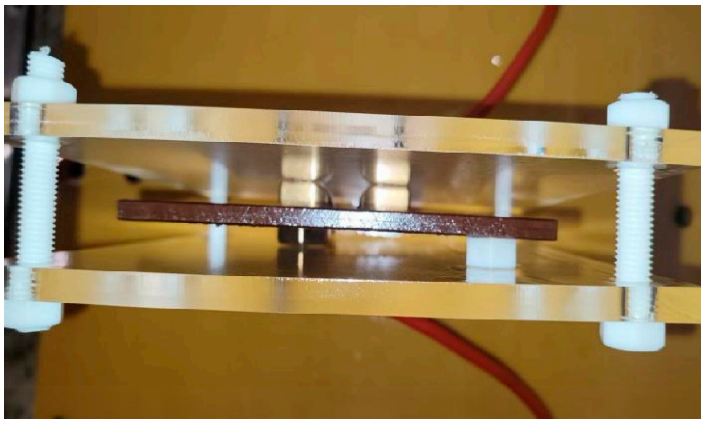


(**a**) Physical photograph of the spacer defect

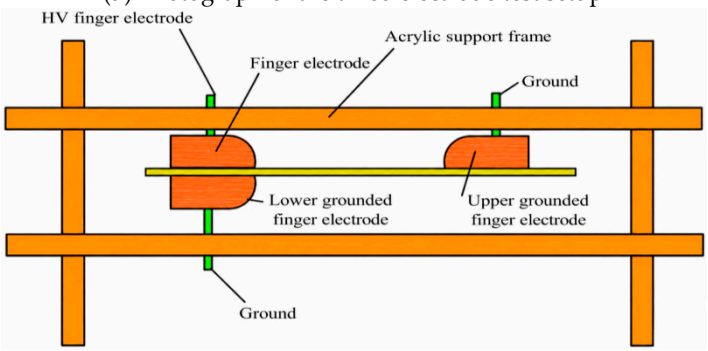


(**b**) Schematic diagram of the spacer defect

Figure 2. Laboratory prototype of spacer defect.



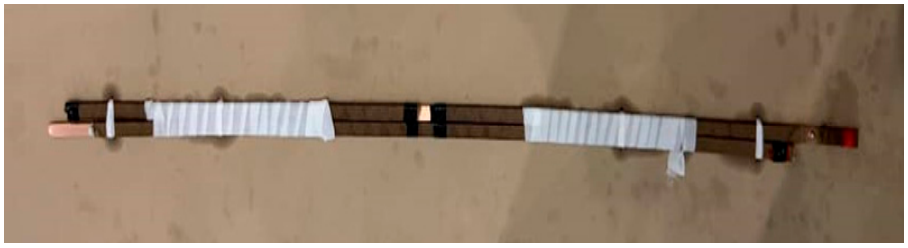
(**a**) Photograph of the three-electrode test setup



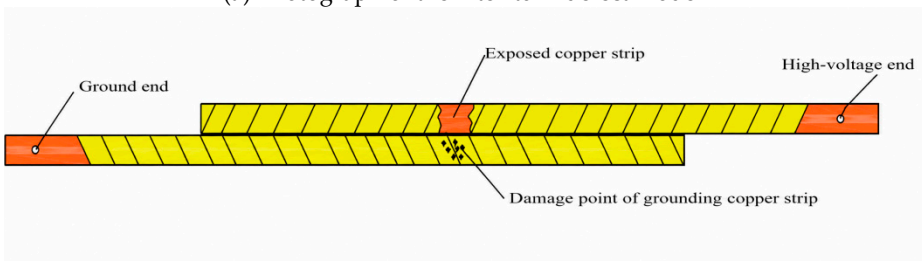
(**b**) Schematic diagram of the three-electrode test setup

Figure 3. Three-electrode test assembly. The yellow bar in (**b**) represents the insulating pressboard specimen used to simulate the spacer defect.

For inter-turn insulation degradation, two 100-cm-long high-voltage inter-turn copper strips taken from a converter transformer were used. For one copper strip, the outer insulation at the central region was completely removed to expose the copper core. A circular hole with a diameter of 4 mm was drilled at one end of the strip to connect the high-voltage terminal. For the other copper strip, the insulation was removed at the position corresponding to the exposed region of the high-voltage copper strip. Similarly, a 4-mm-diameter circular hole was drilled at the end opposite to the high-voltage connection side of the first copper strip and connected to the ground wire, as shown in Figure 4a. Its schematic diagram is shown in Figure 4b.



(**a**) Photograph of the inter-turn defect model



(**b**) Schematic diagram of the inter-turn defect model

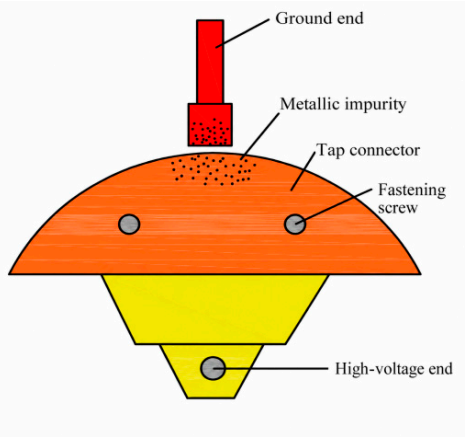
Figure 4. Laboratory model of inter-turn defect. In (**b**), the yellow regions represent the insulation layers surrounding the copper strips, the orange-red regions represent the exposed copper conductors, and the black marks indicate the damaged insulation area of the grounding copper strip.

For floating-potential discharge in the tap changer, a tap selector valve and a metal clamp were taken from a 35 kV transformer tap changer. Metal powder was dispersed inside the experimental container to simulate floating-potential discharge near the tap changer caused by metallic contaminants during the actual operation of a converter transformer, as shown in Figure 5a. Its schematic diagram is shown in Figure 5b.



(**a**) Photograph of the tap changer defect model

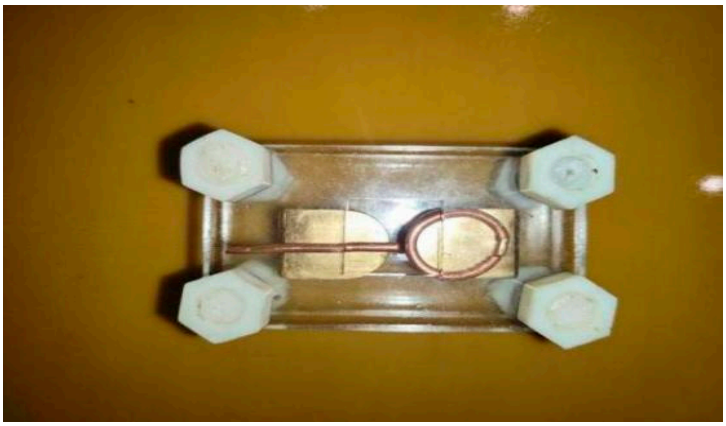
Figure 5. *Cont.*



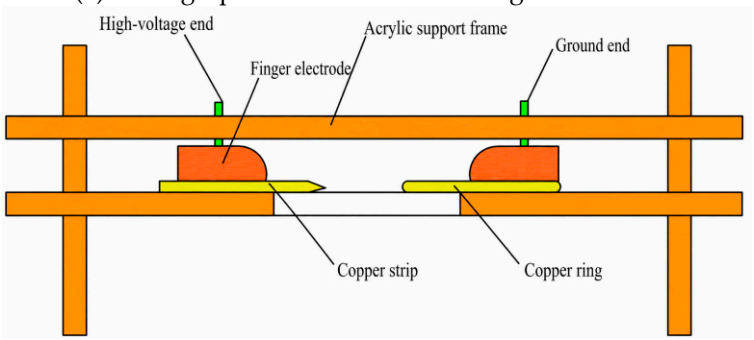
(**b**) Schematic diagram of the tap changer defect model

Figure 5. Laboratory-simulated model of tap changer defect. In (**b**), the red region represents the grounding terminal, the orange region represents the tap connector, and the yellow region represents the lower part of the tap-changer assembly connected to the high-voltage terminal. The black dots indicate metallic impurities, while the gray circles represent the fastening screws and the high-voltage connection point.

A copper strip with an inner diameter of 2 mm and a length of 30 mm, together with a copper ring with an inner diameter of 2 mm, was selected as the test material. To simulate the aging-induced cracking condition of the electrostatic ring, a gap of 1 mm was maintained between the tip of the copper strip and the copper ring, as shown in Figure 6a. Its schematic diagram is shown in Figure 6b.



(**a**) Photograph of the electrostatic ring defect model



(**b**) Schematic diagram of the electrostatic ring defect model

Figure 6. Electrode assembly for electrostatic ring defect simulation experiment.

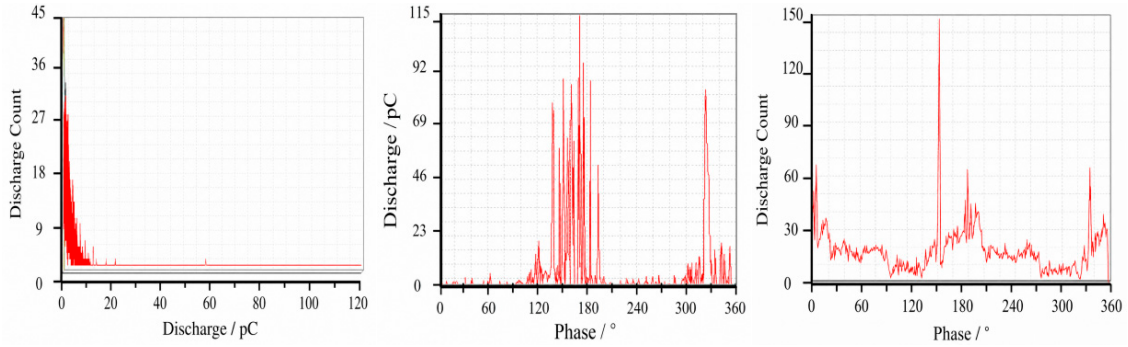
2.3. Experimental Procedure

A 35 kV transformer tank was used as the experimental container and filled with No. 45 transformer insulating oil. The experiments were conducted at ambient temperature, and the moisture content of the insulating oil was maintained within the limits specified by the GB/T 7595 standard [27]. In converter transformers, the tap changer is subjected only to an AC electric field, whereas the insulation structures of the spacer, inter-turn region, and electrostatic ring are exposed to both pure AC and combined AC/DC electric fields. Therefore, a pure AC voltage excitation was applied to the tap changer defect model. For the spacer, inter-turn, and electrostatic ring defect models, both pure AC voltage and combined AC/DC voltage excitations were applied, respectively, to simulate the actual operating conditions of converter transformers.

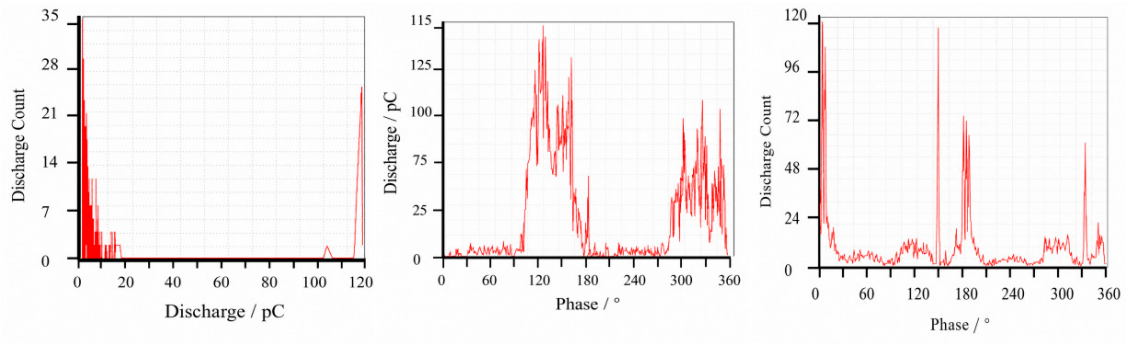
The voltage was applied using a stepwise voltage-raising method [18,19]. Taking the spacer defect model as an example, the pretreated sample was immersed in insulating oil and subjected to a pure AC voltage test, as well as combined AC/DC voltage tests with AC/DC voltage ratios of 1:1, 1:3, 1:5, and 1:7, respectively. In the pure AC test, the voltage was increased stepwise with an increment of 1 kV. In the combined AC/DC voltage tests, the AC voltage increment was adjusted according to the specified voltage ratio, so that the total voltage amplitude increment (AC + DC) remained constant at 1 kV. Each voltage level was maintained for 5 min. After the PD signal was first detected, the voltage was further increased, and the sample entered the discharge development stage, characterized by a steady increase in both discharge magnitude and discharge repetition rate. In the later stage of discharge development, when the sample approached breakdown, it entered the dangerous PD stage. At this stage, the discharge magnitude and discharge repetition rate increased to approximately four to five times those observed during the discharge development stage, and discharges occurred over the full phase range of 0°~360°. Therefore, the experiment was terminated immediately once a sharp increase in discharge magnitude and discharge repetition rate was observed. The experimental procedures for the inter-turn, tap changer, and electrostatic ring defect models were consistent with the above process.

2.4. Partial Discharge Signal Acquisition and Processing

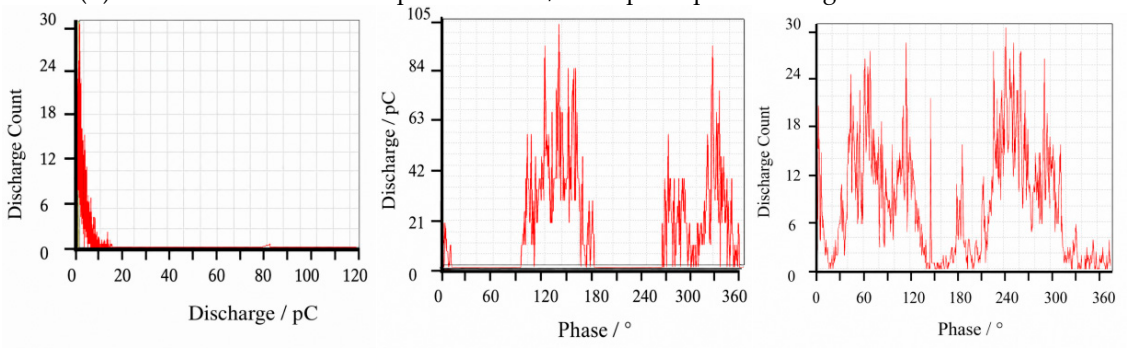
In this study, the PD signals were acquired using a multi-channel digital PD detector (Model GSJFY-3000, Wuhan Guoshi Electric Equipment Co., Ltd., Wuhan, China). The amplifier frequency band was set to 40 kHz–300 kHz, and the signal sampling rate was 100 MS/s. Since the occurrence of PD is closely related to the instantaneous phase of the applied AC voltage, the acquired signals are processed in synchronization with the voltage phase. This results in Phase-Resolved Partial Discharge (PRPD) patterns, which are essential for analyzing discharge characteristics and identifying defect types. Specifically, three types of two-dimensional PRPD spectra were obtained for the four defect models under different electric-field conditions, namely discharge magnitude–discharge repetition number (q-n), phase–discharge magnitude (φ-q), and phase–discharge repetition number (φ-n) spectra. In this experimental study, the three defect models were subjected to combined AC/DC electric-field excitations with four different voltage ratios, resulting in a large number of PD characteristic patterns. Owing to space limitations, for the defect models requiring AC/DC superimposed voltage tests, only the PD characteristic patterns obtained under an AC/DC voltage ratio of 1:1 are selected and presented in this paper, as shown in Figure 7.



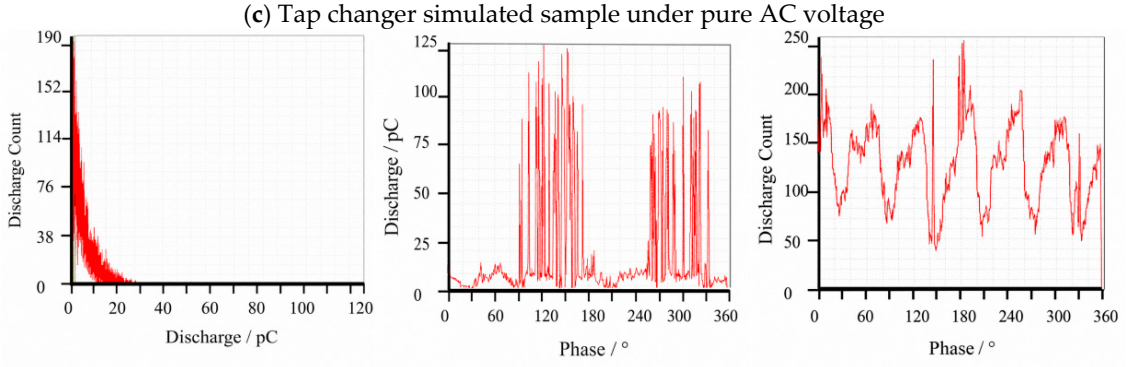
(**a**) Spacer simulated sample under AC/DC superimposed voltage with a ratio of 1:1



(**b**) Inter-turn simulated sample under AC/DC superimposed voltage with a ratio of 1:1



(**c**) Tap changer simulated sample under pure AC voltage



(**d**) Electrostatic ring simulated sample under AC/DC superimposed voltage with a ratio of 1:1

Figure 7. Partial discharge characteristic signals.

Prior to the formal experiments, the background noise level of the high-voltage laboratory was measured to be 10 pC. To ensure signal quality, software-based wavelet denoising was applied to eliminate environmental interference. The specific image preprocessing steps for the CNN model are described in Section 3.2, which include background removal, cropping (removing regions below 10 pC), grayscale conversion, and size normalization to further suppress noise and adapt the data for the CNN model.

For the spacer defect, burrs and sharp protrusions generated at the scratched and cracked regions can easily lead to electric field concentration, thereby inducing PD. Under the AC/DC superimposed voltage test condition with a voltage ratio of 1:1, the discharge phase in the positive half-cycle is mainly distributed within 120°~180°, while that in the negative half-cycle is concentrated within 180°~200°. The discharge magnitude reaches its maximum near 180°, approximately 115 pC, and decreases gradually toward both sides with this phase as the center.

For inter-turn insulation degradation, surface damage was introduced on the outermost insulating paper to form a directional discharge channel. When current flowed through the copper strip, the damage to the external insulation caused electric-field distortion, and discharge first occurred at the insulation weak point. Under the AC/DC superimposed voltage with a voltage ratio of 1:1, discharges in the positive half-cycle were concentrated within 0°~20° and 120°~160°, whereas those in the negative half-cycle were mainly distributed within 320°~360°, with a discharge magnitude of approximately 125 pC.

For floating potential discharge in the tap changer, metallic particles around the tap changer and core clamps can cause electric-field concentration, thereby inducing PD. Under pure AC voltage, discharges in the positive half-cycle are mainly concentrated within 20°~120°, whereas those in the negative half-cycle are concentrated within 220°~320°. The peak discharge magnitude is approximately 86 pC in the positive half-cycle and 105 pC in the negative half-cycle, indicating that the overall discharge magnitude in the positive half-cycle is lower than that in the negative half-cycle.

For tip discharge of the electrostatic ring, a metallic protrusion was introduced at the end of the copper strip to simulate the metal protruding structure caused by cracking of the electrostatic ring. The electric field at the tip is highly distorted, thereby inducing PD. Under the AC/DC superimposed voltage with a voltage ratio of 1:1, discharges in the positive half-cycle are mainly concentrated within 60°~180°, whereas those in the negative half-cycle are concentrated within 250°~340°. The discharge magnitude in the positive half-cycle is slightly higher than that in the negative half-cycle.

To provide a more intuitive comparison and summarize the physical observations, the key characteristic parameters of the PRPD patterns are systematically extracted for the four typical defects. These parameters include the phase distribution ranges in both positive and negative half-cycles, the peak discharge magnitudes, and the corresponding polarity effects. A comprehensive summary of these features under pure AC and combined AC/DC voltages is presented in Table 1. This comparison clearly highlights the distinguishable discharge characteristics of different defect types, laying a solid foundation for the subsequent CNN-based pattern recognition.

Table 1. Summary of PRPD pattern characteristics for the four typical insulation defects under different voltage conditions.

Defect Type	Voltage Condition	Positive Half-Cycle (Phase/Magnitude)	Negative Half-Cycle (Phase/Magnitude)	Polarity Effect (Asymmetry)
Spacer defect	1:1 AC/DC composite	120°–180° (Max ~115 pC at 180°)	180°–200°	Symmetrical distribution (decreasing towards both sides)
Inter-turn defect	1:1 AC/DC composite	0°–20° and 120°–160° (~125 pC)	320°–360°	Stable double peaks in both half-cycles
Tap changer defect	Pure AC	20°–120° (Peak ~86 pC)	220°–320° (Peak ~105 pC)	Negative half-cycle magnitude is slightly higher
Electrostatic ring defect	1:1 AC/DC composite	60°–180°	250°–340°	Positive half-cycle magnitude is slightly higher

By analyzing the PD spectra of the four defect models under pure AC voltage and AC/DC superimposed voltages with different ratios, a total of 48 groups of discharge images were obtained, including q-n, φ-q, and φ-n spectra. The results indicate that the discharge characteristics of different defect models vary significantly under different electric-field conditions and exhibit a high degree of distinguishability. Therefore, methods such as convolutional neural networks can be further employed to achieve automatic recognition and classification of defect types.

3. Partial Discharge Feature Recognition

3.1. Structure and Operation of the Convolutional Neural Network

As a core deep learning model in the field of image recognition, the convolutional neural network (CNN) is based on the fundamental concepts of local receptive fields, weight sharing, and pooling-based dimensionality reduction. Through multilayer feature extraction and nonlinear transformation, CNNs enable end-to-end mapping from raw image pixels to semantic categories. The complete image recognition process generally follows a standardized pipeline, including data preprocessing, convolutional neural network feature extraction, pooling-based feature dimensionality reduction, nonlinear activation transformation, fully connected feature fusion, classification output, and loss optimization. Each stage performs rigorous mathematical operations to progressively abstract and represent image features, ultimately achieving high-accuracy image classification and recognition. Before performing the image recognition task, the raw input images are first subjected to standardized preprocessing. For color images, the image is decomposed into three two-dimensional pixel matrices corresponding to the red, green, and blue channels. For grayscale images, the image is directly converted into a single-channel two-dimensional matrix. To eliminate the influence of pixel-value scale differences on model training, pixel normalization is adopted to map the original pixel values in the range of [0, 255] to [0, 1] or [−1, 1]. The normalization formula is expressed as follows:

$$x_{norm} = \frac{x - x_{\min}}{x_{\max} - x_{\min}} \tag{1}$$

where x denotes the original pixel value, and x_{min} and x_{max} represent the minimum and maximum pixel values of the image, respectively. Meanwhile, the images are cropped or resized to a uniform size according to the task requirements, ensuring that the dimensionality of the input data matches the requirements of the network input layer. This provides a solid data foundation for the subsequent convolution operations.

After data preprocessing, the input image data are fed into the convolutional layers for core feature extraction. In the convolutional layers, multiple learnable convolution kernels perform local convolution operations on the input feature maps, enabling hierarchical extraction of low-level features such as edges, textures, and contours, and progressively transforming them into high-level semantic features.

For multi-channel input images, the convolution operation is performed by weighted summation along the channel dimension, which can be expressed as follows:

$$O_k(i,j) = \sum_{c=0}^{C-1} \sum_{m=0}^{H-1} \sum_{n=0}^{W-1} I_c(i+m, j+n) \cdot K_{k,c}(m,n) + b_k \tag{2}$$

where C is the number of input channels, $K_{k,c}$ denotes the sub-kernel of the *k-th* convolution kernel corresponding to the *c-th* input channel, and O_k represents the output feature map generated by the k-$_{\text{th}}$ convolution kernel. The weight-sharing mechanism allows the same convolution kernel to share parameters across the entire feature map, thereby substantially

reducing the number of model parameters while improving computational efficiency and model generalization capability.

After the convolution operation, the output feature maps are fed into the pooling layer for feature dimensionality reduction and information compression. The pooling layer replaces the original local pixel set with statistical features extracted from local regions, thereby reducing the dimensionality of the feature maps while retaining key feature information and alleviating the computational burden of the model. The average-pooling operation can be expressed as follows:

$$P(i,j) = \frac{1}{S \times S} \sum_{m=0}^{S-1} \sum_{n=0}^{S-1} O(i \times s + m, j \times s + n) \quad (3)$$

where $P(i,j)$ denotes the pooled feature value, S represents the pooling kernel size, and s denotes the pooling stride. Max pooling preserves the most prominent features within a local region, whereas average pooling extracts the mean feature response of the local region. Both operations can effectively reduce the feature dimensionality and subsequent computational cost, while also helping to suppress model overfitting.

The network constructed in this study is a two-level feedforward neural network. Compared with a single-layer network structure, the two-level network can significantly improve recognition accuracy. By alternately stacking convolutional layers and nonlinear activation modules, the network progressively learns and represents hierarchical features from raw data, ranging from low-level details to high-level semantic information. Its architecture is shown in Figure 8 and consists of an input layer, Convolution Layer 1, Max Pooling Layer 1, Convolution Layer 2, Max Pooling Layer 2, a fully connected layer, and an output layer.

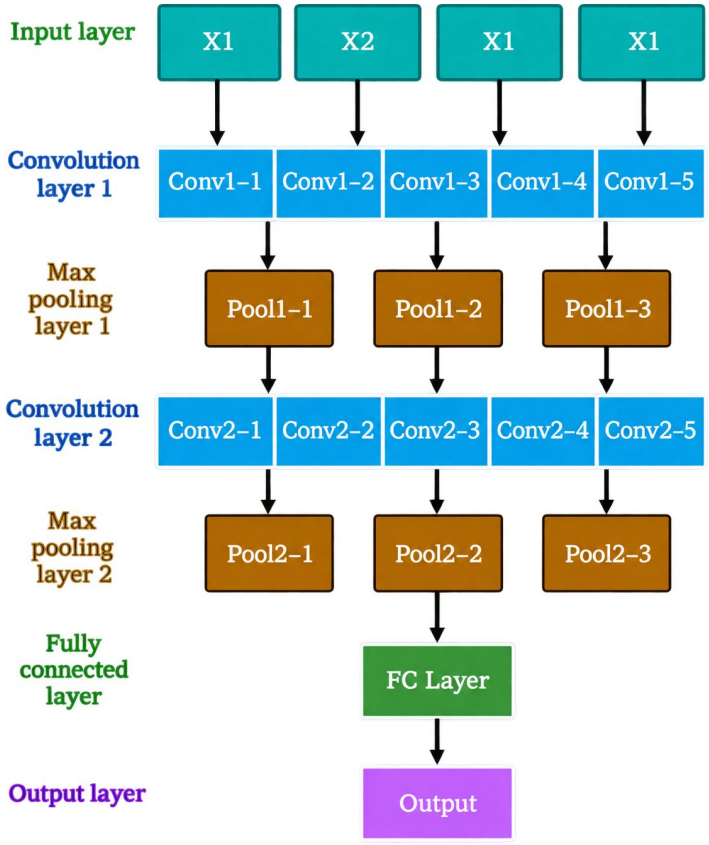
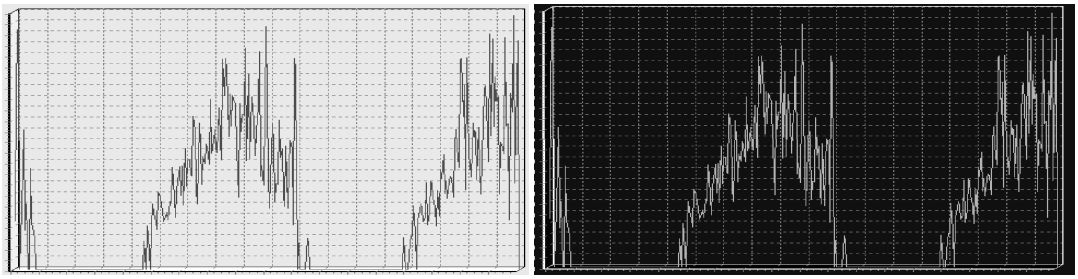


Figure 8. Convolutional neural network architecture.

3.2. Spectrum Preprocessing and Model Construction

Before the images are fed into the convolutional neural network, the original spectra need to be preprocessed to eliminate the influence of interfering information on the computational process. The preprocessing procedure adopted in this study mainly consists of three steps: image cropping, grayscale conversion, and size normalization. As shown in Figure 9, the raw PRPD patterns primarily contain background interference and low-intensity environmental noise. After preprocessing, the background interference is removed, and regions with discharge magnitudes below 10 pC are cropped, ensuring that the model focuses exclusively on the key discharge features. Grayscale conversion further reduces the data volume to one-third of the original, significantly lowering computational complexity, while size normalization standardizes all images to a uniform dimension for CNN input.



(**a**) PRPD pattern before preprocessing (**b**) PRPD pattern after preprocessing

Figure 9. PRPD patterns before and after preprocessing.

The convolutional neural network model constructed in this study consists of one input layer, two convolutional layers, two pooling layers, one fully connected layer, and one output layer. The input layer accepts PRPD spectrogram images of size 256 × 256 × 3, taking the preprocessed three-channel data as input. The two convolutional layers employ 16 kernels of size 9 × 9 and 32 kernels of size 5 × 5. The output of each convolutional layer is first processed by batch normalization and ReLU activation, and then fed into a 2 × 2 max-pooling layer for feature map downsampling. After multiple rounds of convolution and pooling operations, the high-dimensional feature tensor is reshaped into a one-dimensional vector and fed into a fully connected layer containing 128 neurons for deep feature fusion and learning. During this process, a dropout mechanism is introduced to suppress overfitting. Subsequently, another fully connected layer maps the extracted features into the category space. Finally, a Softmax classifier, which is suitable for multi-class classification tasks, outputs the probability distribution corresponding to each category, thereby realizing automatic classification and recognition of PRPD images.

3.3. Training of the Convolutional Neural Network

The dataset used for CNN training and testing was established based on experimentally measured samples. Specifically, 1800 image samples were obtained for each defect category, resulting in a total of 7200 samples. These samples were randomly divided into a training set (84%, 1500 samples per category) and a test set (16%, 300 samples per category). The detailed data classification is listed in Table 2.

Table 2. Data classification.

Category	Category Label	Training Set (Samples)	Test Set (Samples)	Total (Samples)
Spacer defect	C1	1500	300	1800
Inter-turn defect	C2	1500	300	1800
Tap changer defect	C3	1500	300	1800
Electrostatic ring defect	C4	1500	300	1800

The organized dataset was classified, and the specific procedure for recognizing the partial discharge patterns of the four types of defects is shown in Figure 10.

(1) The PD data were preprocessed to construct the raw feature dataset of PD signals.
(2) The above feature dataset was divided into a training set and a test set, with the training set accounting for 84% and the test set accounting for 16%.
(3) The divided datasets were standardized to unify the data scales, thereby reducing the learning complexity of the model and improving system robustness.
(4) After standardization, the training set was input into the neural network. Through forward and backward propagation, the data features were identified and extracted, and the network parameters were optimized to complete network training.
(5) After training, the test set was input into the trained neural network for performance evaluation.

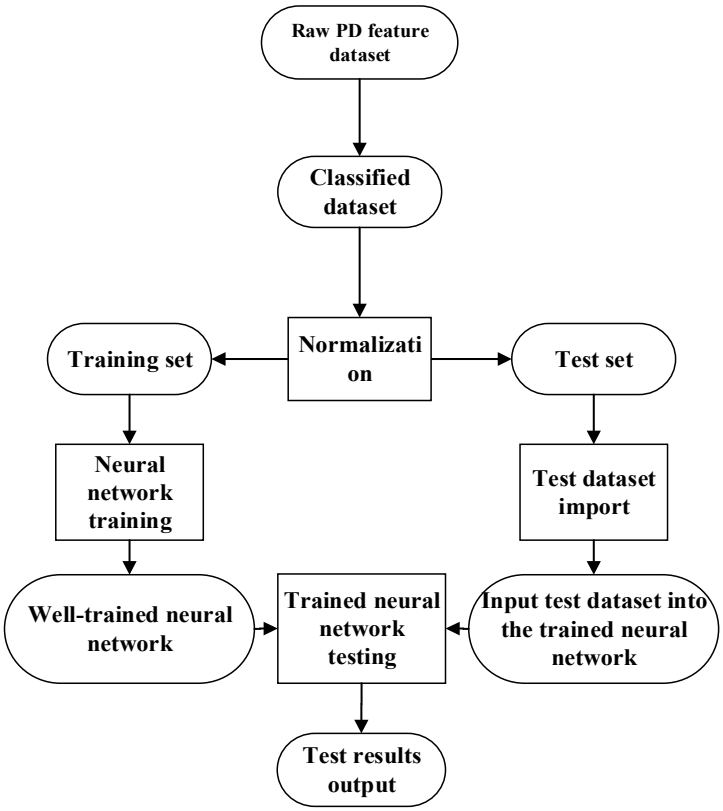


Figure 10. Flowchart of neural network training and testing. The oval shapes represent datasets, model states, and output results, while the rectangular shapes represent data processing, neural network training, and testing operations.

The overall classification accuracy of the proposed CNN model is calculated as the total number of correctly classified samples divided by the total number of test samples

across all categories. Since each defect category contains exactly 300 test samples, the overall accuracy is 93.7%, which is mathematically equivalent to the arithmetic mean of the individual accuracies shown in the diagonal of the confusion matrix. The selection of 300 test samples per category is based on the standard 84%/16% split ratio, which provides a balanced evaluation across all four defect categories. Furthermore, to assess the repeatability of the proposed model, the training and testing processes were repeated multiple times. The experimental results showed minor fluctuations, and the overall accuracy was close to the reported 93.7%. The deep neural network was trained and tested according to the procedure shown in Figure 10. The final results are presented in the form of a confusion matrix, as shown in Figure 11.

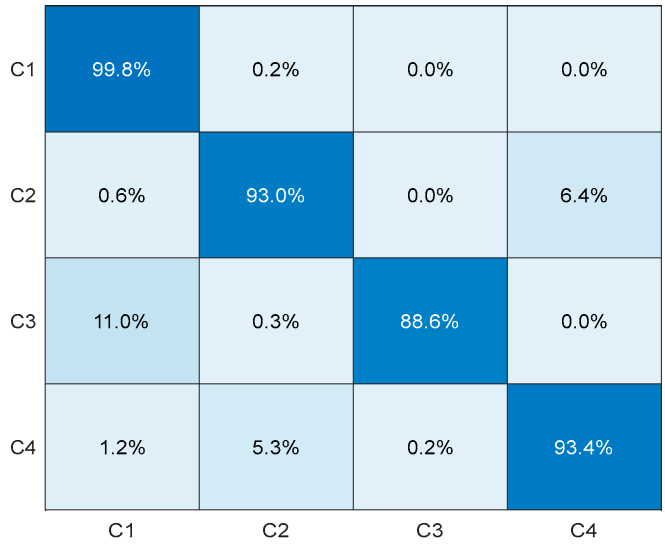


Figure 11. Confusion matrix for CNN-Based recognition. Different shades of blue represent the classification percentages. Darker blue indicates higher percentages, while lighter blue indicates lower percentages. The diagonal elements represent correctly classified samples, whereas the off-diagonal elements indicate misclassifications.

It should be noted that the recognition accuracy of the tap changer defect (C3) is relatively lower at 88.6%. This is primarily attributed to two reasons: (1) The PD characteristics of the tap changer defect (C3) and the spacer defect (C1) share similarities in the negative half-cycle regarding phase distribution and discharge magnitude, leading to a certain degree of misclassification. (2) The field samples of the tap changer defect exhibited higher variability under actual operating conditions.

4. Field Case Analysis

The trained convolutional neural network (CNN) model was applied to the diagnosis of on-site insulation defects in a ±400 kV converter transformer (Shandong Dachi Electric Co., Ltd. (Heze, China)). An inter-turn insulation defect model and a tap changer defect model were arranged at the corresponding positions inside the converter transformer, as shown in Figure 12. After the defect models were installed, on-site PD tests and measurements were carried out. In this test, a PD detection system developed by Baoding Huachuang was employed. The system can acquire PD signals through multiple detection methods and obtain key information such as discharge amplitude and spectrum waveforms. It also supports the storage and reading of two-dimensional and three-dimensional spectra, thereby enabling effective evaluation of the internal PD state of converter transformers.



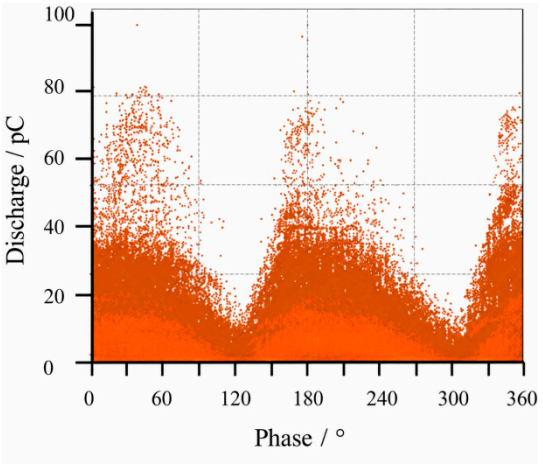
(**a**) Installation position of the inter-turn defect model (**b**) Installation position of the tap changer defect model

Figure 12. Internal fault model placement point of converter transformer.

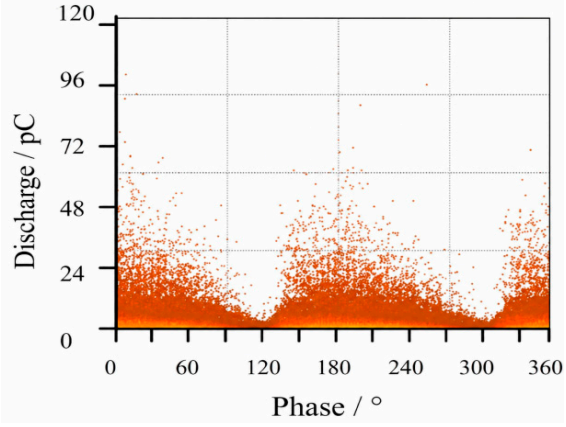
Through on-site detection, PRPD patterns corresponding to the preset internal faults of the converter transformer were successfully obtained, as shown in Figure 13. Owing to the complexity of the field testing environment, the acquired PRPD patterns contained noise signals caused by environmental interference and equipment self-interference. To avoid the influence of noise on the judgment accuracy of the CNN model, the PRPD patterns were preprocessed, including noise filtering and signal normalization. This ensured that the preprocessed PRPD patterns could accurately reflect the fault characteristics and remain consistent with the input data format and feature dimensions used during CNN model training, thereby providing reliable support for accurate model diagnosis. It should be noted that the PRPD data in Figure 13 was acquired in strict synchronization with the applied voltage phase via hardware triggering.

The preprocessed PRPD patterns were input into the fully trained convolutional neural network (CNN)-based fault classification model for validation testing. The field validation was conducted on a ±400 kV converter transformer, where a total of 500 field samples were collected under actual operating conditions for the two preset defects. Based on these 500 field samples, the experimental results show that the recognition accuracy of the model for the preset inter-turn insulation defect was 95%, indicating effective identification of PD caused by insulation damage. For the tap changer defect, the recognition accuracy reached 96.3%, demonstrating that the model can accurately identify PD signals induced by internal metallic particles. The classification results therefore exhibit a high level of reliability.

Based on the overall field application test process and results, the CNN-based fault classification model can effectively extract fault features from PRPD patterns of PD under the actual operating conditions of a ±400 kV converter transformer. The model achieves high recognition accuracy for the two typical internal faults, providing a rapid and accurate diagnostic basis for converter transformer insulation assessment. Therefore, the proposed CNN-based fault classification model demonstrates certain engineering applicability under practical operating conditions of converter transformers and can be further extended to routine insulation diagnosis of converter transformers, thereby improving the efficiency and reliability of fault early warning and diagnosis.



(**a**) Field-tested PRPD pattern of the inter-turn defect



(**b**) Field-tested PRPD pattern of the tap changer defect

Figure 13. Field-tested PRPD patterns for (**a**) inter-turn defect and (**b**) tap changer defect.

5. Conclusions

Based on the structural characteristics of converter transformers, four typical defect models were constructed in this study. The physical mechanisms and discharge characteristics of PD associated with each defect were analyzed, and PD tests were carried out to establish a discharge feature database. Finally, fault classification was achieved through neural-network-based recognition. The main conclusions are as follows:

In the discharge tests, the four fault models exhibited distinct discharge characteristics. For the spacer defect, discharges were mainly concentrated near the phase angle of 180° and showed a symmetrical distribution. For the inter-turn defect, stable double peaks appeared in both the positive and negative half-cycles. The tap changer defect also exhibited a double-peak distribution, with relatively wide and nearly symmetrical phase distributions in the positive and negative half-cycles; however, the discharge magnitude and distribution range in the negative half-cycle were slightly higher. For the electrostatic ring defect, discharges in the positive and negative half-cycles were concentrated in different phase regions, and the discharge magnitude in the positive half-cycle was slightly higher.

A convolutional neural network (CNN)-based method was adopted for deep learning and recognition of PD features. An image dataset was constructed using three types of PRPD patterns (q-n, φ-q, φ-n) obtained from the four laboratory test samples, and the CNN model achieved an overall recognition accuracy of 93.7% for spacer, inter-turn, electrostatic ring, and tap changer defects. This demonstrates that the proposed method can effectively identify the types of PD in laboratory models of converter transformers.

The trained CNN model was further applied to field validation on a ±400 kV converter transformer, achieving recognition accuracies of 95% and 96.3% for inter-turn and tap changer defects, respectively. However, several limitations should be noted. The field validation was limited to only two typical defect types with a restricted number of field samples, and the severe electromagnetic interference in the on-site environment presents challenges for model generalization. Future work will focus on expanding the field sample database, handling overlapping defect features, and integrating the CNN model into online monitoring systems for converter transformers.

Author Contributions: Conceptualization, Y.T. and Y.H.; methodology, Y.T.; software, Y.H.; validation, Y.H., H.L. and J.L.; formal analysis, Y.T.; investigation, Y.T., J.L. and H.Y.; resources, H.L.; data curation, Y.T.; writing—original draft preparation, Y.T. and Y.H.; writing—review and editing, M.C.; visualization, Y.T.; supervision, M.C.; project administration, M.C.; funding acquisition, M.C. All authors have read and agreed to the published version of the manuscript.

Funding: This research was funded by the North China Branch of State Grid Corporation of China, grant number 529923240003.

Data Availability Statement: The data presented in this study are available on request from the corresponding author. The data are not publicly available due to confidentiality restrictions associated with the research project.

Conflicts of Interest: Authors Yunpeng Tang, Jian Liu, Hong Liu, and Hua Yu were employed by the State Grid Corporation of China. The remaining authors declare that the research was conducted in the absence of any commercial or financial relationships that could be construed as a potential conflict of interest.

References

1. Gao, S.; Zhao, J.; Qiao, H.; Tian, Y.; Wang, Y.; Yin, Y. Review on Partial Discharge Detection and Characteristics of Converter Transformers. *Insul. Mater.* **2022**, *55*, 1–9. [CrossRef]
2. Li, P.; Gu, C.; Chen, D.; He, H.W.; Huang, R.P.; Xie, L.; Chen, X.J.; Ding, Y.J.; Xie, L. Preliminary research on ±1500 kV ultra-high voltage direct current transmission technology. *High Volt. Eng.* **2017**, *43*, 3139–3148.
3. Liu, Z.; Zhang, Q.; Dong, C.; Zhang, L.; Wang, Z. Research on Large-Scale, High-Efficiency, and Safe Transmission of Wind, Solar, and Thermal Power from Major Energy Bases via Ultra-High Voltage Direct Current. *Proc. CSEE* **2014**, *34*, 2513–2522.
4. Tang, G.; Luo, X.; Wei, X. Multi-terminal DC transmission and DC grid technology. *Proc. CSEE* **2013**, *33*, 8–17.
5. Tang, G.; He, Z.; Pang, H. Research, Application and Development of Flexible DC Transmission Engineering Technology. *Autom. Electr. Power Syst.* **2013**, *37*, 3–14. [CrossRef]
6. Du, B.; Zhu, W.; Li, J.; Jiang, J. Current Research Status on Oil-Paper Insulation of Converter Transformer Valve Side Bushings. *Trans. China Electrotech. Soc.* **2019**, *34*, 1300–1309.
7. Liang, C.; Deng, J.; Zhou, H.; Zhang, J.; Liu, Q.; Pan, Z. Typical insulation defect cases of converter transformers. *Transformer* **2019**, *56*, 80–84.
8. Du, B.; Jiang, J. Review on the Effect of Moisture in Oil-Paper Insulation of Converter Transformers on Partial Discharge Behavior. *High Volt. Eng.* **2021**, *47*, 2932–2945.
9. Qiao, M. Research on Online Monitoring System for Partial Discharge in Converter Transformers. Master's Thesis, Shandong University, Jinan, China, 2020.
10. Sun, W.; Yang, L.; Zare, F.; Xia, Y.W.; Cheng, L.; Zhou, K. 3D modeling of an HVDC converter transformer and its application on the electrical field of windings subject to voltage harmonics. *Int. J. Electr. Power Energy Syst.* **2020**, *117*, 105581. [CrossRef]
11. Dong, M.; Kou, X.; Yao, D.; Yao, Y.; Wang, W.; Zhang, Y.; Tang, J. Study on the Aggregation Characteristics of Metal Particles and Local Discharge Characteristics in Transformer Oil Under AC/DC Composite Voltage. *Insul. Mater.* **2022**, *55*, 74–79.
12. Qian, G.; Zhang, N.; Hao, J.; Dai, W.; Wu, J. Effect of power-frequency superimposed harmonic voltage composite stress on partial discharge characteristics and breakdown failure patterns in oil-paper insulation. *High Volt. Eng.* **2026**, *52*, 1750–1762.
13. Yue, B.; Cao, Y. Structural Optimization of the Voltage Regulation Winding in Ultra-High Voltage Converter Transformers and Its Simulation and Experimental Verification. *Transformer* **2022**, *59*, 51–54+70.
14. Li, J. Research on an Intelligent Diagnosis Method for Transformer Partial Discharge Based on Deep Learning. Master's Thesis, North China Electric Power University, Beijing, China, 2023.

15. Qu, W.; Zhao, H.; Liu, H.; Feng, X.; Zhao, T.; Zhang, K. Research on Anti-interference Technology for High-frequency Online Monitoring of Partial Discharge in Converter Transformers. *Transformer* **2022**, *59*, 43–50.
16. Li, J.; Wang, L.; Bao, Z.; Huang, X.; Wang, S. On-site localization and diagnosis of partial discharge faults in ultra-high voltage converter transformers. *Power Syst. Equip.* **2021**, 106–108.
17. Shao, M.; Qi, B.; Zheng, S.; Ma, C.; Liu, W.; Huang, H.; Li, C. Simulation study on the electromagnetic wave propagation law of partial discharge in valve-side bushings of converter transformers. *Proc. CSEE* **2024**, *44*, 5398–5408.
18. Jia, J.; Tao, F.; Yang, Q.; Fu, H.; Yang, J.; Lu, Y.; Zhao, H. Research on transformer partial discharge localization methods under complex multipath propagation conditions. *Proc. CSEE* **2022**, *42*, 5338–5348.
19. Wang, W.; Yang, D.-D.; Li, R.; Yan, L.; Guo, R.-Z.; Zhang, N.; Tao, W.-B. On-site partial discharge test technology of converter transformer. *J. Eng.* **2019**, *2019*, 1820–1823. [CrossRef]
20. Liu, F.; Nie, D.; Peng, Q.; Deng, J.; Yao, X.; Zhang, L. Cluster-based identification of DC partial discharge defects in oil-paper insulation of converter transformers. *Transformer* **2014**, *51*, 54–58.
21. Si, W.; Li, S.; Xiao, H.; Li, Q.; Shi, Y.; Zhang, T. Defect Pattern Recognition Based on Partial Discharge Characteristics of Oil-Pressboard Insulation for UHVDC Converter Transformer. *Energies* **2018**, *11*, 592. [CrossRef]
22. Wei, Z.; Qi, B.; Zuo, J.; Li, C. A method for diagnosing oil-paper insulation defects in converter transformers based on partial discharge image features. *Power Syst. Technol.* **2015**, *39*, 1160–1166.
23. Karthik Prabhu, D.; Maheswari, R.V.; Vigneshwaran, B. Deep Learning Based Power Transformer Monitoring Using Partial Discharge Patterns. *Intell. Autom. Soft Comput.* **2022**, *34*, 1441–1454. [CrossRef]
24. Zhang, Y. Deep Learning-Based Localized Discharge Identification in Transformers and Its Incremental Learning Strategy. Ph.D. Thesis, North China Electric Power University, Beijing, China, 2023.
25. Zhang, Q.; Song, H.; Jiang, Y.; Chen, Y.; Sheng, G.; Jiang, X. Pattern recognition of transformer partial discharge based on OS-ELM. *High Volt. Eng.* **2018**, *44*, 1122–1130.
26. Chen, J.; Zhou, Y.; Bai, Z.; Zhao, Y.; Zhang, Y.; Zhang, L. A method for partial discharge pattern recognition in oil-paper insulation based on multi-channel convolutional neural networks. *High Volt. Eng.* **2022**, *48*, 1705–1715.
27. *GB/T 7595-2017*; Quality of Transformer Oils in Service. Standards Press of China: Beijing, China, 2017.

Disclaimer/Publisher's Note: The statements, opinions and data contained in all publications are solely those of the individual author(s) and contributor(s) and not of MDPI and/or the editor(s). MDPI and/or the editor(s) disclaim responsibility for any injury to people or property resulting from any ideas, methods, instructions or products referred to in the content.